A comparison of kinematic and dynamic schemes for calculating long-range atmospheric trajectories

by

Allison Schneider

Submitted to the Dept. of Earth, Atmospheric and Planetary Sciences
in partial fulfillment of the requirements for the degree of

Bachelor of Science in Earth, Atmospheric and Planetary Sciences

at the

MASSACHUSETTS INSTITUTE OF TECHNOLOGY

September 2017

Author ..... Signature redacted
Dept. of Earth, Atmospheric and Planetary Sciences
August 28, 2017

Certified by..... Signature redacted .....
Glenn R. Flierl
Professor of Oceanography
Thesis Supervisor

Accepted by ..... Signature redacted .....
Richard P. Binzel
Chairman, Committee on Undergraduate Program

A comparison of kinematic and dynamic schemes for calculating long-range atmospheric trajectories

by

Allison Schneider

Submitted to the Dept. of Earth, Atmospheric and Planetary Sciences
on August 28, 2017, in partial fulfillment of the
requirements for the degree of
Bachelor of Science in Earth, Atmospheric and Planetary Sciences

Abstract

Two numerical models, one kinematic and one dynamic, were created and compared in their ability to predict trajectories of atmospheric parcels over eight days. While kinematic models are more widely used due to their accuracy, dynamic models can be used pedagogically to visualize the balance of forces in the atmosphere. The kinematic model used gridded wind speed data from the Global Forecast System (GFS) to predict parcel flow, while the dynamic model calculated wind speeds from advection equations using geopotential height fields from GFS. The trajectories of ensembles of parcels were simulated from five launch locations. The spread of parcels from each location was calculated along with the deviation from reference trajectories. The dynamic model performed comparably to the kinematic model, despite the presence of inertial oscillations in some computed trajectories at mid- and high- latitudes which are likely to be physically unrealistic. The dynamic model was more sensitive to changes in spatial resolution than the kinematic model. Dynamic trajectory models were shown to be accurate enough to be used as a tool to visualize the interplay of forces acting in the atmosphere.

Thesis Supervisor: Glenn R. Flierl
Title: Professor of Oceanography

Acknowledgments

I'd like to thank Glenn Flierl for guidance and many patient blackboard explanations;
Bill McKenna, for equal parts practical and poetic insight;
Jane Connor, for all she's taught me about science communication;
Vicki McKenna, for her invaluable support of EAPS and especially of me;
Adam Strandberg, for knowing more about statistics and myself than I do;
Gabe Duquette, for a writing refuge and for convincing me that I'd finish the writing;
And my family, for everything.

Contents

List of Figures

List of Tables

1 Introduction

Knowing which way the wind blows has a wide range of applications in atmospheric science. Predicting the weather, modeling the climate, and tracking the spread of air pollution all benefit from the development of trajectory models that describe the paths of parcels of air [Stohl, 1998]. Since Petterssen [1940] introduced a graphical technique for computing trajectories, the methods studied have grown more diverse and complex, and have taken advantage of new sources of atmospheric data from observations and climate models.

In the family tree of trajectory prediction schemes, one of the first branching points is between kinematic and dynamic models. Kinematic models use the wind speed to predict trajectories, treating the tracked parcels as massless entities going with the flow. The accuracy of kinematic models has been improved in recent decades by the availability of high-resolution wind speed data output by global forecast models [Stohl and Seibert, 1998]. While kinematic models take wind speeds as input, dynamic models calculate wind speeds along the trajectory. Dynamic models take atmospheric mass field information as input and use differential equations to compute the changing velocities of parcels. Dynamic models have been popular due to their consistency using atmospheric data sampled at long time intervals; however, now that high-resolution atmospheric data is more readily available, kinematic models are more common [Stohl, 1998].

An unexplored potential use for dynamic trajectory models is visualizing the balance of forces in the atmosphere. The equations for calculating changes in parcel velocity use the sum of forces on a parcel per unit mass. Dynamic trajectory models link a topic presented in introductory physics classes—force balance—to topics often

not encountered until later—fluid dynamics and motion in a rotating system. If a simple dynamic model can be shown to produce acceptably accurate trajectories, it might be used to demonstrate how basic physical principles interact to produce the complex behavior of the atmosphere.

1.1 The Aerocene project

A model for this kind of demonstration is the Aerocene project's float predictor tool, developed by Glenn Flierl, Lodovico Illari, and Bill McKenna of MIT's Department of Earth, Atmospheric and Planetary Sciences. The Aerocene project is the work of Tomás Saraceno, the inaugural Visiting Artist at the MIT Center for Art, Science & Technology (CAST). The project consists of a fleet of solar-powered hot air balloons which came about as a result of the artist's interest in zero-carbon-emission flight of all kinds [Saraceno et al., 2015].

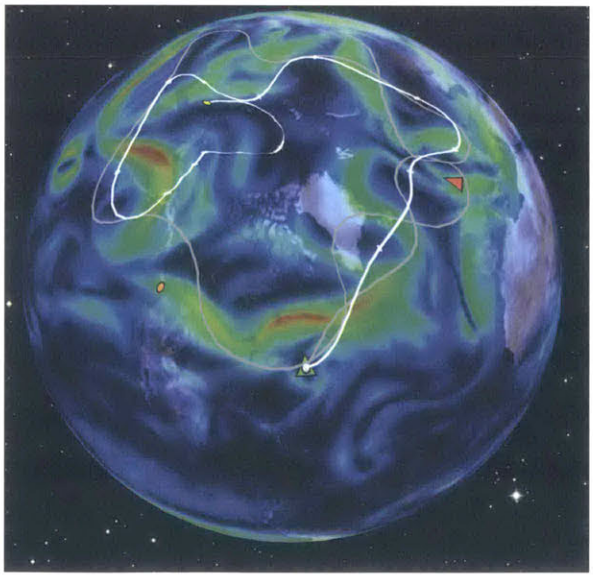

Figure 1-1: The Aerocene project's float predictor tool at float.aerocene.org.

The float predictor web app, available at float.aerocene.org, is a kinematic trajectory model used to visualize the paths of these solar balloons launched from any given location. A sample trajectory is shown in Figure 1-1. The tool has been used in public demonstrations about the Aerocene project to great success: it provides a

way to explore the characteristics of atmospheric flow in different regions of the Earth without requiring any knowledge of the physics involved.

Using a dynamic model to calculate trajectories would allow a similar tool to be built which visualizes the balance of forces along a parcel's trajectory. The goal of this project is to determine whether a dynamic model can be created that accurately represents the general behavior of atmospheric parcels. A dynamic model and a kinematic model will be built, and the dynamic trajectories will be compared both to those calculated by the kinematic model and to reference trajectories calculated by an existing model. In this next section, the equations that comprise the dynamic model will be derived.

1.2 Acceleration and velocity from geopotential height

The models developed here will be two-dimensional isobaric, meaning parcels are assumed to stay on a surface of constant pressure. This is often not true in the atmosphere, but the assumption simplifies calculation and isobaric trajectories are accurate enough for some applications [Stohl and Seibert, 1998]. In a dynamic isobaric trajectory model, the acceleration of a parcel of air at a given pressure level can be determined from its velocity, latitude, and geopotential height. The geopotential height Z_g of a surface of pressure p above mean sea level is

$$Z_g(p) = R \int_p^{p_s} \frac{T}{g} \frac{dp}{p}, \tag{1.1}$$

where R is the gas constant, T is temperature, p_s is surface pressure, g is acceleration due to gravity at mean sea level, and $Z_g(p_s)$ is set to 0. In the troposphere, the region in which trajectories will be studied, the difference between the geopotential height and the actual height of a pressure level is negligible [Marshall and Plumb, 2008].

The geopotential Φ is the potential energy of the Earth's gravitational field at a height h:

$$\Phi(h) = gZ_g(h). \tag{1.2}$$

The full equation for acceleration of an air parcel in the atmosphere is

$$\frac{D\vec{u}}{Dt} + \frac{1}{\rho}\nabla p + \nabla\Phi + f\hat{z} \times \vec{u} = \mathcal{F}, \tag{1.3}$$

where $\vec{u}$ is the wind velocity vector, ρ is the density of air, f is the Coriolis parameter, and $\mathcal{F}$ is the force of friction per unit mass [Marshall and Plumb, 2008]. The Coriolis parameter f measures the effect of the Earth's rotation speed Ω at a given latitude φ:

$$f = 2\Omega \sin\varphi. \tag{1.4}$$

To implement Equation 1.3 in the dynamic model, it must be written in terms of the zonal (west-east), meridional (north-south), and vertical wind components u, v and w. If the model assumes that friction is negligible at the studied pressure level, $\mathcal{F}$ is taken to be zero.

$$\frac{Du}{Dt} + \frac{1}{\rho}\frac{\partial p}{\partial x} - fv = 0 \tag{1.5}$$

$$\frac{Dv}{Dt} + \frac{1}{\rho}\frac{\partial p}{\partial y} - fu = 0 \tag{1.6}$$

$$\frac{Dw}{Dt} + \frac{1}{\rho}\frac{\partial p}{\partial z} + g = 0. \tag{1.7}$$

The derivative of the geopotential is zero in the horizontal directions, and equal to g in the vertical following from Equation 1.2. Using the hydrostatic approximation, the vertical velocity is zero, so Equation 1.7 becomes an expression of hydrostatic

equilibrium:

$$\frac{1}{\rho}\frac{\partial p}{\partial z} + g = 0, \text{ or} \tag{1.8}$$

$$\frac{\partial p}{\partial z} = -\rho g. \tag{1.9}$$

Pressure can be defined as a function of the horizontal position and the geopotential height of a particular isobar at that position at a given time:

$$p(x, y, Z_g(x, y, t), t) = p_0 \tag{1.10}$$

where p_0 is the selected pressure level. The partial derivatives of pressure with respect to x and y are

$$\frac{\partial p}{\partial x} + \frac{\partial p}{\partial Z_g}\frac{\partial Z_g}{\partial x} = 0 \tag{1.11}$$

$$\frac{\partial p}{\partial y} + \frac{\partial p}{\partial Z_g}\frac{\partial Z_g}{\partial y} = 0. \tag{1.12}$$

Using the hydrostatic relationship in Equation 1.9, these become

$$\frac{\partial p}{\partial x} = \rho g \frac{\partial Z_g}{\partial x} \tag{1.13}$$

$$\frac{\partial p}{\partial y} = \rho g \frac{\partial Z_g}{\partial y} \tag{1.14}$$

which can be substituted into Equations 1.5 and 1.6 to yield

$$\frac{Du}{Dt} = fv - g\frac{\partial Z_g}{\partial x} \tag{1.15}$$

$$\frac{Dv}{Dt} = -fu - f\frac{\partial Z_g}{\partial y}. \tag{1.16}$$

In pressure coordinates, the total derivative is

$$\frac{D}{Dt} = \frac{\partial}{\partial t} + u\frac{\partial}{\partial x} + v\frac{\partial}{\partial y} + \omega\frac{\partial}{\partial p}, \tag{1.17}$$

where ω is the pressure coordinate vertical velocity Dp/Dt. According to the isobaric assumption of the model, $\omega = 0$, so this becomes

$$\frac{D}{Dt} = \frac{\partial}{\partial t} + u\frac{\partial}{\partial x} + v\frac{\partial}{\partial y}. \tag{1.18}$$

This derivative applied to the position vector $\vec{X}$, in x and y components, is

$$\frac{Dx}{Dt} = u \tag{1.19}$$

$$\frac{Dy}{Dt} = v. \tag{1.20}$$

The dynamic model uses Equations 1.15 and 1.16 to calculate velocity and Equations 1.19 and 1.20 to calculate position at each timestep. The kinematic model retrieves precomputed wind velocities, so only requires Equations 1.19 and 1.20 to calculate position.

2 Methods

Two trajectory calculation routines, a kinematic and a dynamic model, were written using Python's NumPy scientific computing package. Both routines numerically predict the trajectories of an ensemble of parcels by determining the velocities of parcels over time. The kinematic routine finds these velocities by interpolating between grids of wind speed data. The dynamic routine calculates velocities using advection equations relating the parcel acceleration and the geopotential height of a given pressure level.

2.1 Eight day dataset

Data from the Global Forecast System (GFS), a weather forecast model produced by the National Centers for Environmental Prediction (NCEP), was used for both models. The dataset chosen was an eight day forecast, starting at 12:00:00 on February 21st, 2017, with predictions at intervals of three hours. Each file in the dataset contains atmospheric predictions for the beginning of a three-hour interval. The values of atmospheric variables are predicted at each point on a latitude-longitude grid spanning the globe, with a spacing between gridpoints of 0.25 degree. Values are predicted for East-West and North-South wind speed components u and v, as well as the geopotential height Z_g of the 250 hectopascal (hPa) pressure level.

Values of Z_g are plotted at intervals of two days in Figure 2-1. Geopotential height of a pressure surface rises from the poles to the Equator because the density of air decreases as temperature rises. Near the Equator, geopotential height is mostly uniform. In the mid-latitudes, a sharper gradient is observed, along with synoptic-

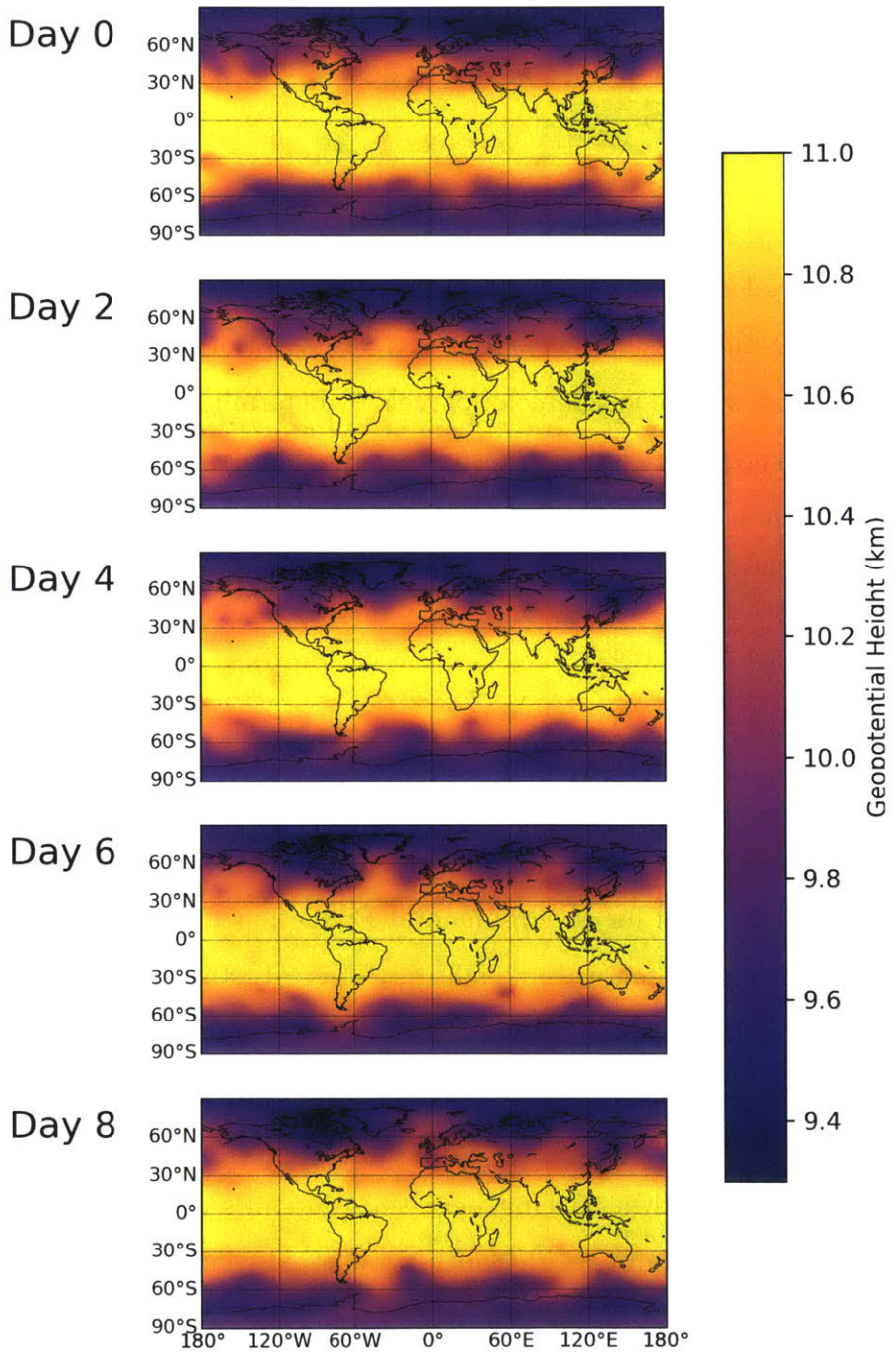

Figure 2-1: Global geopotential height of the 250 hPa pressure surface plotted every two days for the duration of the experiment.

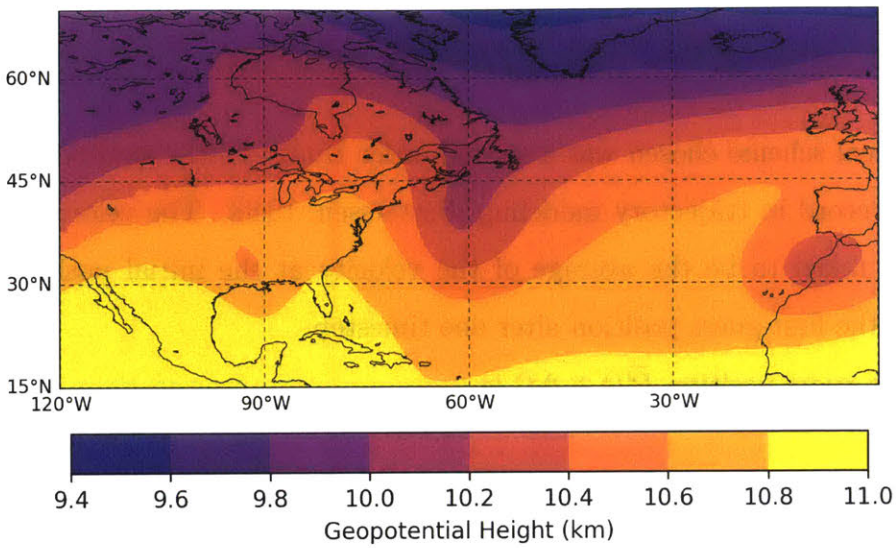

Figure 2-2: A cold front descends from the north at 60°W at the initial time of the experiment.

scale variation associated with weather systems. Figure 2-2 shows an example of mid-latitude eddies. A cold front, marked by lower geopotential height, can be seen advancing south at 60°W. The cyclonic rotation developing between this cold front and the warm front to the west are indicative of a high pressure system.

2.2 Linear interpolation

Both the kinematic and dynamic models require an interpolation scheme to produce values for atmospheric variables at positions between the gridded values provided by GFS. Linear interpolation is the standard choice for trajectory models [Bowman et al., 2013]. For both models, linear interpolation was used in three dimensions (latitude, longitude, and time). In the kinematic model, u and v components of wind speed were interpolated to the current positions of the air parcels, while in the dynamic model, geopotential height was interpolated.

2.3 Second-order integration scheme

The numerical scheme chosen was a second-order Runge-Kutta method which has a long track record in trajectory modeling [Petterssen, 1940]. The velocity at a given timestep is taken to be the average of the velocity at the initial position and the velocity at the first-guess position after one timestep.

The first guess position $\vec{P}'(t + \Delta t)$ is

$$\vec{P}'(t + \Delta t) = \vec{P}(t) + \vec{V}(\vec{P}, t)\Delta t \tag{2.1}$$

and the final position $\vec{P}(t + \Delta t)$ is

$$\vec{P}(t + \Delta t) = \vec{P}(t) + \frac{1}{2}\left[\vec{V}(\vec{P}, t) + \vec{V}(\vec{P}', t + \Delta t)\right]\Delta t \tag{2.2}$$

where $\vec{P}$ is a position vector with latitude and longitude components, and $\vec{V}$ a velocity vector with u and v wind speeds [Draxler and Hess, 1997]. This integration method is used by HYSPLIT and a number of other trajectory models, including FLEXPART, LAGRANTO, and STILT [Bowman et al., 2013, Stein et al., 2015] For trajectories calculated from interpolated gridded wind velocities, higher order integration schemes do not add precision [Draxler and Hess, 1997].

2.4 Constant timestep

For simplicity, both models employ a constant timestep. To save computation, HYSPLIT uses a dynamic timestep, varying from one minute to one hour, computed to satisfy

$$U_{max}[\text{grid-units min}^{-1}]\Delta t[\text{min}] < 0.75[\text{grid-units}] \tag{2.3}$$

[Draxler and Hess, 1997]. This ensures that the parcel does not blow past any grid

squares during a single timestep, which maximizes the accuracy of the calculation. The value of the constant timestep for the experimental models was chosen so that Equation 2.3 is always satisfied. The process of choosing the timestep is detailed in Section 3.3.

2.5 Spatial resolutions of 0.25° and 0.5°

The native resolution of the GFS data is 0.25° per grid square. In order to explore the effect of spatial data resolution on calculated trajectories, model runs were performed using this resolution and a lower resolution of 0.5°. For the 0.5° model runs, every other data point in the latitude and longitude directions was discarded, creating a data grid with half the original resolution.

2.6 Kinematic equations

At each timestep, after u and v speeds were interpolated and an average value found using the integration scheme, the kinematic model used two equations to solve for a parcel's displacement. The equations convert u and v provided by GFS in meters per second to time derivatives of latitude and longitude in radians. The r value of a parcel is taken to be the radius of the Earth R_E plus the parcel's geopotential height Z_g.

$$r = R_E + Z_g \tag{2.4}$$

$$\frac{d\varphi}{dt} = \frac{v}{r} \tag{2.5}$$

$$\frac{d\lambda}{dt} = \frac{u}{r\cos\varphi} \tag{2.6}$$

The initial conditions for these equations (latitude and longitude) are specified by choosing the initial position of a parcel.

2.7 Dynamic equations

In the dynamic model, velocity at the next timestep was calculated using advection equations which incorporate the current geopotential height gradient and the previous timestep's u and v values. Standard acceleration due to gravity is g.

$$f = 2\Omega \sin\varphi \tag{2.7}$$

$$\frac{du}{dt} = fv - \frac{g}{r\cos\varphi}\frac{\partial Z_g}{\partial \lambda} \tag{2.8}$$

$$\frac{dv}{dt} = -fu - \frac{g}{r}\frac{\partial Z_g}{\partial \varphi} \tag{2.9}$$

Equations 2.8 and 2.9 are equations 1.15 and 1.16 transformed to geographic coordinates. After velocity at the next timestep is determined, the dynamic model also uses kinematic equations 2.5 and 2.6 to find the parcel position. This system of four differential equations requires four initial conditions: initial zonal and meridional velocities are needed in addition to initial latitude and longitude. Initial velocity components are set as the geostrophic wind at the initial position,

$$u_g = \frac{-g}{f}\frac{\partial Z_g}{\partial \varphi}\frac{1}{r} \tag{2.10}$$

$$v_g = \frac{g}{f}\frac{\partial Z_g}{\partial \lambda}\frac{1}{r\cos\varphi}. \tag{2.11}$$

2.8 The root-mean-square deviation measures parcel spread

For an ensemble of parcels, variance among trajectories over time was measured by calculating the mean trajectory: the path of an imaginary parcel whose position at each timestep is the average of the parcels' positions. At each timestep, the root-

mean-square deviation (RMSD) is the square root of the average squared value of each particle's distance from the mean trajectory.

The mean trajectory was determined by finding the centroids of parcel positions at each timestep after converting trajectory latitudes and longitudes to three-dimensional Cartesian coordinates. NumPy's `arctan2(y,x)` is a two-argument arctangent function with a range of $(-\pi, \pi]$, N is the number of parcels, and n is the parcel index.

$$x_n = \cos\varphi_n \cos\lambda_n \qquad \bar{x} = \frac{1}{N}\sum_{n=1}^{N} x_n \tag{2.12}$$

$$y_n = \cos\varphi_n \sin\lambda_n \qquad \bar{y} = \frac{1}{N}\sum_{n=1}^{N} y_n \tag{2.13}$$

$$z_n = \sin\varphi_n \qquad \bar{z} = \frac{1}{N}\sum_{n=1}^{N} z_n \tag{2.14}$$

$$\bar{\lambda} \doteq \operatorname{arctan2}(\bar{y}, \bar{x}) \tag{2.15}$$

$$\bar{\varphi} = \operatorname{arctan2}(\bar{z}, \sqrt{\bar{x}^2 + \bar{y}^2}) \tag{2.16}$$

The distance d between each parcel (with position φ_n, λ_n) and the mean parcel was calculated with the haversine formula

$$\Delta\varphi_n = |\varphi_n - \bar{\varphi}| \tag{2.17}$$

$$\Delta\lambda_n = |\lambda_n - \bar{\lambda}| \tag{2.18}$$

$$a_n = \sin^2\left(\frac{\Delta\varphi_n}{2}\right) + \cos\varphi_n \cos\bar{\varphi} \sin^2\left(\frac{\Delta\lambda_n}{2}\right) \tag{2.19}$$

$$c_n = 2 \cdot \operatorname{arctan2}(\sqrt{a_n}, \sqrt{1 - a_n}) \tag{2.20}$$

$$d_n = R_E \cdot c_n \tag{2.21}$$

which is accurate and well-conditioned for small angles [Sinnott, 1984]. The RMSD at each timestep is calculated using the distance between each parcel and the mean

parcel.

$$\mathrm{RMSD}\,(t) = \sqrt{\sum_{n=1}^{N} \frac{d_n(t)^2}{N}} \tag{2.22}$$

2.9 The absolute and relative horizontal transport deviation measure accuracy

Because the RMSD uses the mean trajectory as a reference value, it measures variance among trajectories of nearby parcels within a model. To compare trajectories between models, however, previous work has defined the absolute and relative horizontal transport deviation measures (AHTD and RHTD) [Stohl, 1998]. In this study, the AHTD is defined as

$$\mathrm{AHTD}\,(t) = \frac{1}{N}\sqrt{\sum_{n=1}^{N} d_n(t)^2} \tag{2.23}$$

This is similar to the RMSD, but the factor of $\frac{1}{N}$ has been moved outside the square root to agree with the standard definition [Kuo et al., 1985, Rolph and Draxler, 1990]. The values for d_n are calculated as in the RMSD, with the mean latitude $\bar{\varphi}$ and longitude $\bar{\lambda}$ in Equations 2.17 and 2.18 replaced by the latitude and longitude of a reference trajectory. The RHTD is the AHTD normalized by a length L_H.

$$\mathrm{RHTD}\,(t) = \frac{\mathrm{AHTD}\,(t)}{L_H} \tag{2.24}$$

In this study, L_H is defined as by Rolph and Draxler as the mean absolute horizontal travel distance of the reference trajectories.

$$L_H = \frac{1}{N} \sum_{n=1}^{N} \sqrt{\sum_{t=\Delta t}^{T} d_n(t)^2}. \tag{2.25}$$

This is a measure of the curved path length of the reference trajectory, not the distance between the starting and ending points as used by Kuo et al. [1985]. Here Δt is the timestep and T is the total trajectory time. Again d_n is calculated as in the RMSD, but with Equations 2.17 and 2.18 replaced by the difference between positions of a single parcel at two different timesteps:

$$\Delta\varphi_n = |\varphi_n(t) - \varphi_n(t - \Delta t)| \tag{2.26}$$

$$\Delta\lambda_n = |\lambda_n(t) - \lambda_n(t - \Delta t)|. \tag{2.27}$$

2.10 Reference trajectories obtained from HYSPLIT

Although the "true" trajectories of parcels from the ten-day study period are unobservable, reference trajectories which approximate them can be calculated. Reference trajectories were obtained using NOAA's Real-time Environmental Applications and Display sYstem (READY), a tool which uses the HYSPLIT model to generate parcel trajectories [Rolph et al., 2017]. Analysis data from the Global Data Assimilation System (GDAS), with a grid spacing of 0.5 degree and time resolution of three hours, was selected as the source of wind field information [NOAA, 2004].

Two kinds of reference trajectories were calculated with HYSPLIT: isobaric and three dimensional. Isobaric trajectories use the same vertical transport assumption as the experimental models. Three-dimensional trajectories model the vertical as well as the horizontal wind.

While the experimental models use pressure as a vertical coordinate, HYSPLIT only accepts parcel height specified in meters above mean sea level (AMSL) or above ground level (AGL). The starting geopotential height of the parcel at the southwest

corner of the experimental trajectory ensemble in each location was used as the starting height. This height was input into HYSPLIT as meters above mean sea level, since geopotential height is defined in relation to mean sea level.

There are a number of differences between the experimental and HYSPLIT models, so the ability of this analysis to ascribe deviations between experimental and reference trajectories to particular sources is limited. One difference is the isobaric assumption of the experimental models compared with the vertical wind modeling of the HYSPLIT 3D model. Comparing the HYSPLIT isobaric reference trajectories to the HYSPLIT 3D trajectories measures the contribution of the isobaric assumption alone to trajectory error. Another difference is the data source: the experimental models use forecast data, while the reference models use HYSPLIT data. A third difference is the timesteps used: constant for the experimental models and variable for HYSPLIT. The time resolution of the data is the same for both the experimental and reference models. Spatial resolution is the same for the 0.5° experimental model runs, and different for the 0.25° model runs.

Fully three-dimensional trajectories and analysis data are more accurate than isobaric trajectories and forecast data, so these factors will make reference trajectories closer to the "true" parcel trajectories than those calculated by the kinematic and dynamic models. [Stohl, 1998]. However, the coarser resolution of the GDAS reanalysis data compared to GFS forecast data may make reference trajectories less accurate.

2.11 Ensembles of parcels launched from five locations

Trajectory behavior was investigated using tightly clustered ensembles of parcels launched from five different locations: These locations were Boston, Massachusetts; Bauru, Brazil; Jakarta, Indonesia; Barrow, Alaska; and Reykjavík, Iceland. Ensembles of 25 parcels arranged in a 5×5 grid spaced at 0.25° intervals were launched from each location: the entire ensemble spanned one square degree. Table 2.1 lists the

Table 2.1: Southwest corners of ensemble launch points.

Location	Label	Latitude	Longitude
Boston	A	41°N	72°W
Bauru	B	23°S	50°W
Jakarta	C	7°S	106°E
Barrow	D	71°N	156°W
Reykjavík	E	64°N	22°W

locations of the parcels at the southwest corner of the ensemble at each location, and Figure 2-3 shows each location on maps of zonal and meridional wind velocity.

These locations were chosen to represent a variety of latitudes and atmospheric wind conditions. As seen in Figure 2-3, Boston is in a region of strong northerly wind at the launch time. Parcels launched from Boston will likely blow south into the subtropical jet visible around 30°N. Bauru is poised between bands of zonal wind blowing in opposite directions, which may cause neighboring parcels to diverge. Jakarta is near the Equator in a region with calm winds in both the zonal and meridional directions. The location with the highest latitude is Barrow, in the calmer region north of the polar jet. Finally, Rejkjavík is around 60°N, and parcels launched here are likely to flow into the polar jet.

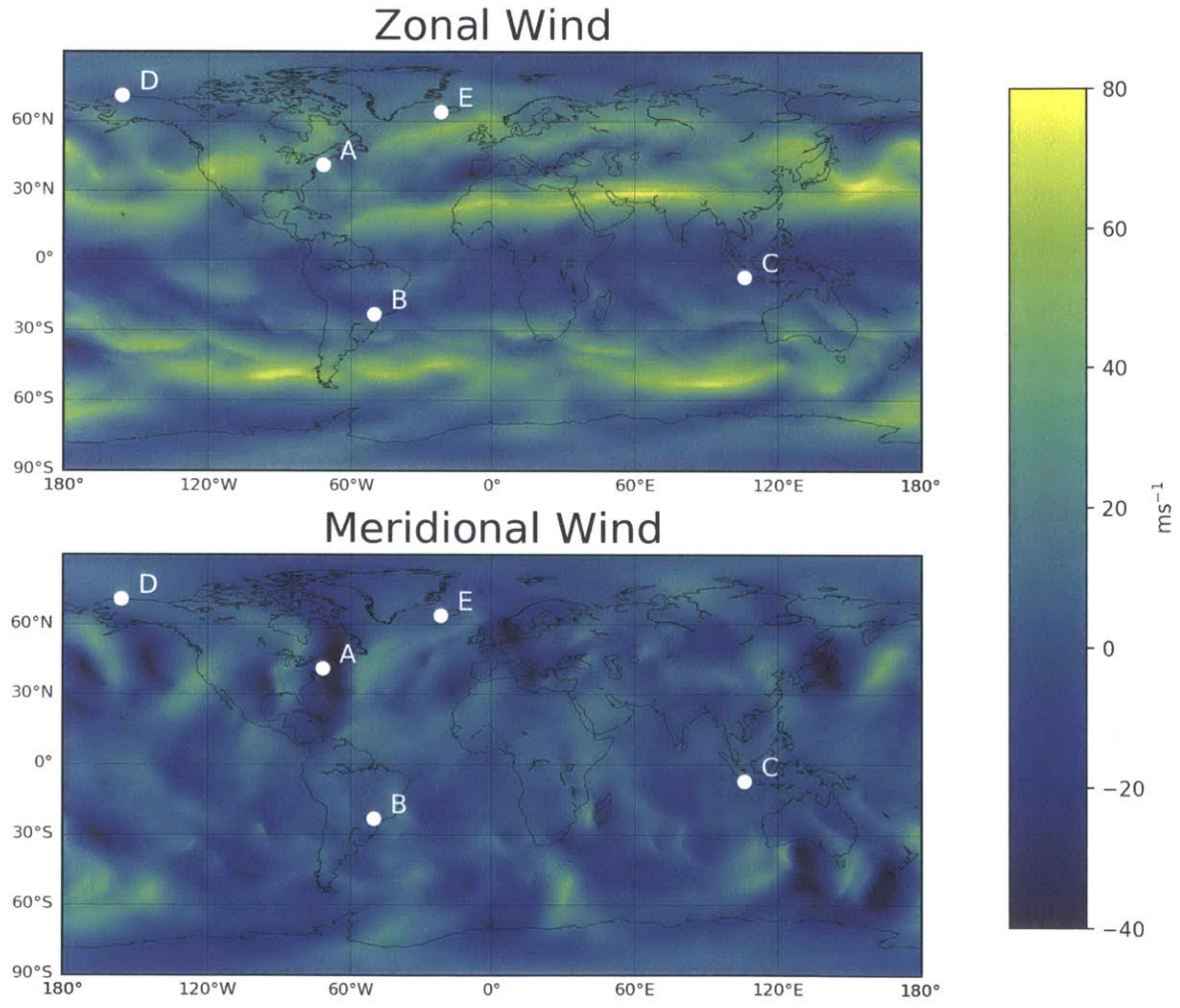

Figure 2-3: Zonal and meridional wind speeds at the time of launch with launch locations.

3 Tuning the models

3.1 Inertial circles in the dynamic model

When the dynamic model was tested, some trajectories traced out large spirals, behavior uncharacteristic of atmospheric flow. Figure 3-1 shows an example of one such trajectory. The parcel's spiral looks like a series of inertial circles, a result of the Coriolis force term in the dynamic equations. In the Northern Hemisphere, the direction of the Coriolis force is to the right of a parcel's motion.

To confirm that these are inertial circles, the period and radius can be observed and compared to theoretically predicted values. As seen in Figure 3-2, the radius of the bolded circle is roughly 9 degrees of latitude, or 1000 kilometers. Inspecting the trajectory data shows that the parcel took 28 hours to complete the circle.

The period T and radius R of an inertial circle are

$$T = \frac{2\pi}{f} \tag{3.1}$$

$$R = \frac{|\vec{u}|}{f} \tag{3.2}$$

where f is the Coriolis parameter. The theoretical radius is obtained by taking the average magnitude of speed along the bolded part of the trajectory. The latitude for f was taken to be 40°N, a latitude in the middle of the circle.

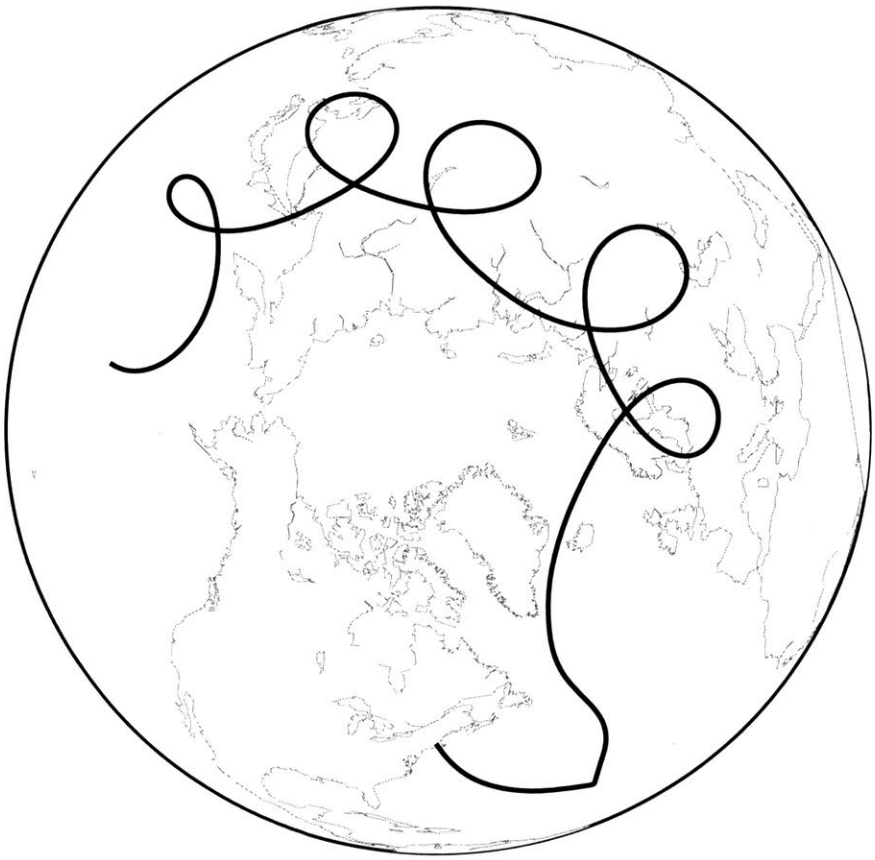

Figure 3-1: A parcel launched from 41.75°N, 71.25°W. Five inertial circles are visible in the latter part of the trajectory.

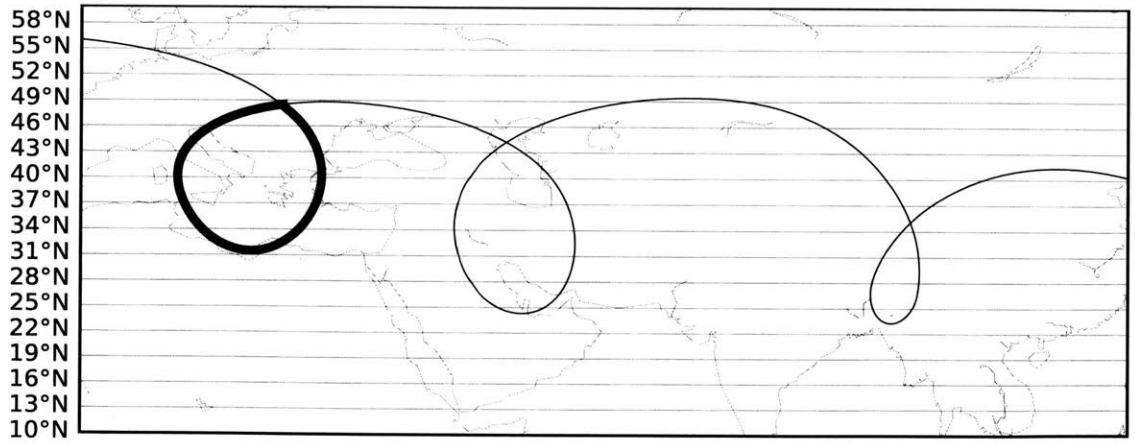

Figure 3-2: A detail view of three of the spirals in Figure 3-1. The bolded circle spans about 18 degrees of latitude.

Table 3.1: Theoretical and observed values for period and radius of one inertial circle.

	Theoretical	Observed
Period	19 hours	28 hours
Radius	420 km	1,000 km

$$R = \frac{|\vec{v}|}{f} = \frac{\sqrt{\bar{u}^2 + \bar{v}^2}}{2\Omega \sin 40^\circ} = 400 \text{ km}. \tag{3.3}$$

The theoretical period is

$$\frac{2\pi}{2\Omega \sin 40^\circ} = 19 \text{ hours}. \tag{3.4}$$

Both observed values are about a factor of two apart from the theoretical values. The order of magnitude similarity suggests that the trajectory spirals can be described as inertial circles. Differences between the theoretical and observed values may stem from variations in the wind in both space and time as well as variations in the Coriolis parameter f along the path.

3.2 Adding friction to the dynamic model

Previous studies have observed inertial circles in trajectories calculated with dynamic models which become particularly apparent for trajectories longer than 24 hours. [Stohl and Seibert, 1998] One approach to mitigating oscillations, used by Stohl and Seibert, is to take a weighted average of the wind speeds from the dynamic model and interpolated wind speeds from a model such as GFS at each timestep. Another approach is to change the frictionless assumption of the dynamical model. The force of friction has the effect of damping oscillations due to inertial motion. Using the definition of geostrophic wind in Equations 2.10 and 2.11, Equations 2.8 and 2.9 with an added friction term become

Figure 3-3: *Left*: Twenty five trajectories calculated with the frictionless dynamic model. Parcels were launched in an evenly-spaced 5x5 grid with its lower-left corner at 41°N, 72°W and upper-right corner at 42°N, 71°W. The large spirals are implausible for jet stream flow and reflect a problem with the model. *Right*: The same parcels with trajectories calculated by the dynamic model with friction. A few parcels still exhibit unrealistic spirals, but in general, trajectories are more plausible.

$$\frac{du}{dt} = f(v - v_g) - r_f(u - u_g) \tag{3.5}$$

$$\frac{dv}{dt} = -f(u - u_g) - r_f(v - v_g). \tag{3.6}$$

The damping term r_f is analogous to the Coriolis parameter: it has units of second^{-1} and is a measure of the force of friction. The value chosen for r_f was 10^{-6} seconds^{-1}, or 0.1 days^{-1}, a rough order of magnitude guess based on the experimental trajectory lengths.

Adding friction terms to the dynamic model reduces inertial oscillations significantly, as demonstrated in Figure 3-3. The terms were added to the dynamic model used in the Results section.

3.3 Choosing a timestep

The threshold that HYSPLIT uses to calculate its dynamic timestep, Equation 2.3, can also be expressed as the difference between a threshold velocity and trajectory velocity. If the trajectory velocity is greater than the threshold velocity at any time, the timestep is too short. Therefore, the conditions for velocity components in the u and v directions are

$$\frac{0.75sm\cos\varphi}{\Delta t} - u(t)_{max} < 0 \tag{3.7}$$

$$\frac{0.75sm}{\Delta t} - v(t)_{max} < 0 \tag{3.8}$$

The maximum fraction of a grid square a parcel should travel in one timestep is 0.75. The spatial resolution, s, is the number of degrees per grid square: for this dataset, 0.25. The conversion factor m between degrees latitude and distance is 111,320 meters.

These differences were plotted along an ensemble of test trajectories: 25 parcels launched in a 5x5 grid around Boston, Massachusetts, between 41°N, 72°W and 42°N, 71°W on February 21st, 2017 at 12:00 UTC. These trajectories were calculated with the kinematic model and the dynamic model with added friction. For both calculation schemes, the parcels can be observed to flow into the subtropical jet, which contains some of the highest windspeeds at the studied pressure level. As a result, a timestep tuned to these parcels should be appropriate for most trajectories. The first timestep tested was three minutes, as shown in Figure 3-4. Zonal speeds for dynamic trajectories surpass the threshold a number of times, indicating that a timestep of three minutes is too long.

The same trajectories were calculated using a shorter timestep of one minute and thirty seconds, as shown in Figure 3-5. Here, velocities are below the threshold at all times along the trajectory. With the exception of two dynamic trajectories, the threshold velocity is at least 50 meters per second greater than the observed velocity.

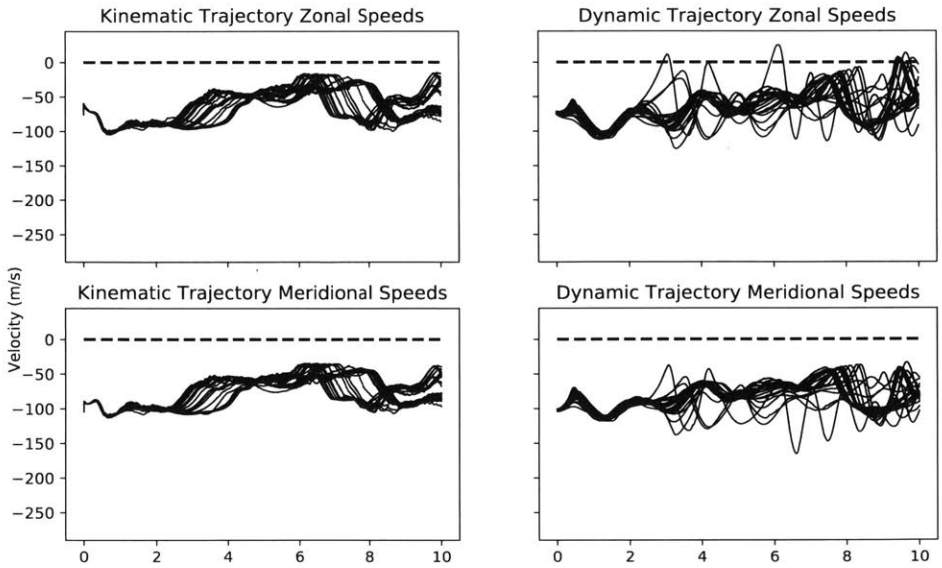

Figure 3-4: For a timestep of 3 minutes, trajectory speed is compared to threshold speed. Solid lines represent the threshold speed minus the trajectory speed. The dashed line at a velocity of zero represents the speed threshold. Note in the upper-right hand plot that the zonal speeds for some trajectories surpass the threshold.

Since one minute and thirty seconds was a sufficiently short timestep for this dataset, it was chosen as the timestep for all other model runs.

3.4 Initializing velocity for the dynamic model

The proposed method for determining initial trajectory velocity in the dynamic model was using the geostrophic wind, as expressed in Equations 2.10 and 2.11. The geostrophic wind is the theoretical wind calculated using the assumption that the Coriolis force balances the pressure gradient force.

This method is attractive for two reasons. For one, it does not require additional data to be added to the dynamic model. Geostrophic wind is calculated using the same grid of geopotential height gradients used for the advection equations 2.8 and 2.9. For another, initializing wind speed with geostrophic wind may reduce the inertial circle behavior observed in the dynamic model, which results from wind speeds deviating from the geostrophic approximation.

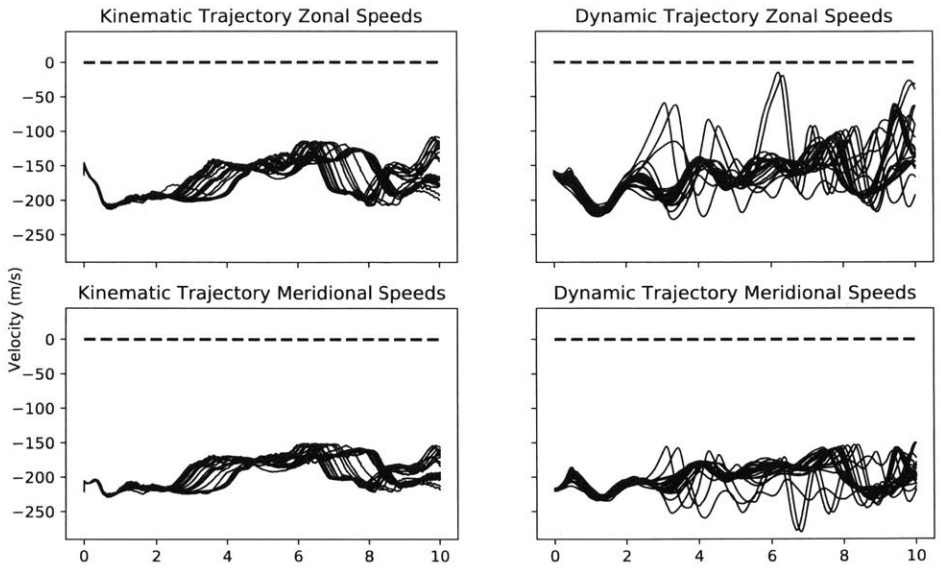

Figure 3-5: For a timestep of 1 minute and 30 seconds, trajectory speed is compared to threshold speed. For this choice of timestep, all parcel velocities are below the threshold.

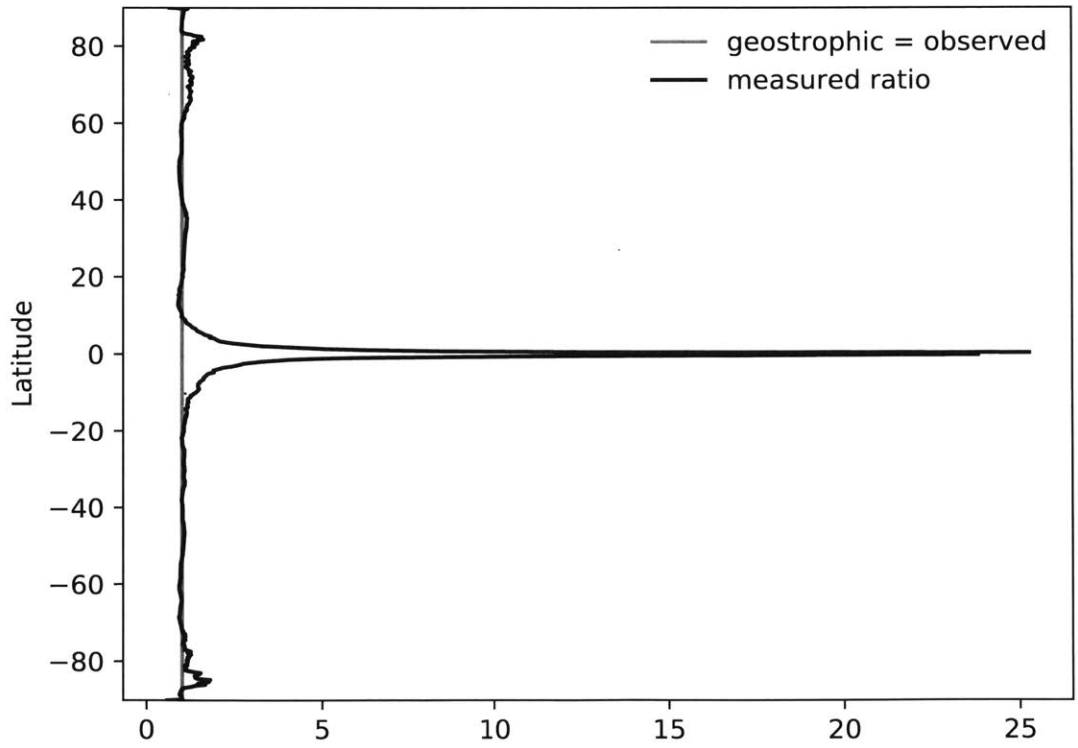

Figure 3-6: The ratio of zonally averaged geostrophic wind speed to zonally averaged gridded wind speed as a function of latitude. Near the Equator, the ratio increases sharply, indicating that the geostrophic approximation is invalid there.

However, the geostrophic approximation of wind speed breaks down near the equator. Figure 3-6 shows the ratio of zonally averaged geostrophic wind speeds to zonally averaged gridded wind speeds at the initial time. For most latitudes, the ratio is close to 1, which indicates that the geostrophic wind is a reasonable assumption. Between 20°S and 20°N, the geostrophic wind becomes much greater than the observed wind. As the latitude goes to zero, the Coriolis parameter f in Equations 2.8 and 2.9 blows up, and the resulting geostrophic wind becomes unphysical.

Trajectories of parcels launched from Bauru, Brazil and Jakarta, Indonesia pass through latitudes where the geostrophic approximation is invalid. For these two locations, velocities were initialized with the gridded wind values at the trajectory start locations instead of geostrophic wind. This may increase inertial circle prevalence, but the initial deviation from the geostrophic wind is damped by the dynamic model's friction term. In addition, the geostrophic wind in the friction term was set to zero for trajectories originating in Bauru and Jakarta. For these model runs, Equations 3.5 and 3.6 were modified to become

$$\frac{du}{dt} = f(v - v_g) - r_f u \tag{3.9}$$

$$\frac{dv}{dt} = -f(u - u_g) - r_f v. \tag{3.10}$$

Because of these changes in wind speed initialization and friction calculation, trajectories from Bauru and Jakarta cannot be directly compared with trajectories from Boston, Rejkjavík and Barrow. Creating a dynamic model that smoothly deals with the transition to equatorial latitudes is a potential direction for future work.

4 Results

The following tables show the root-mean-square deviation, absolute horizontal trajectory deviation, and relative horizontal trajectory deviation for the five ensembles of parcels. Tables 4.1, 4.3, 4.5, 4.7, and 4.9 contain data from the experimental trajectories at each location for grid resolutions of 0.25° and 0.5°. The bar chart in Figure 4-1 is a visual representation of this data. Tables 4.2, 4.4, 4.6, 4.8, and 4.10 show these measures for the HYSPLIT reference trajectories, which were calculated with 0.5° resolution analysis data. Confidence intervals of 95% were calculated assuming a χ^2 distribution with 24 degrees of freedom.

Figures 4-2 through 4-8 contain maps of trajectories from each launch location, calculated by the kinematic and dynamic models at both resolutions as well as HYSPLIT 3D and isobaric models. Trajectories from Barrow and Reykjavík are plotted on equidistant cylindrical maps, for comparison to other trajectories, and on polar stereographic maps, for a clearer view of parcel flow.

Table 4.1: Boston measures of transport deviation after eight days.

Resolution	Statistic	Model	Reference	Value	95% CI
0.25°	RMSD	kinematic	mean trajectory	1,800 km	1,400–2,500 km
		dynamic	mean trajectory	3,100 km	2,400–4,300 km
	AHTD	kinematic	HYSPLIT 3D	2,600 km	2,000–3,600 km
		dynamic	HYSPLIT 3D	2,600 km	2,000–3,600 km
		kinematic	HYSPLIT isobaric	950 km	740–1,300 km
		dynamic	HYSPLIT isobaric	1,100 km	860–1,500 km
	RHTD	kinematic	HYSPLIT 3D	2.1	1.6–2.9
		dynamic	HYSPLIT 3D	2.1	1.7–2.9
		kinematic	HYSPLIT isobaric	0.15	0.12–0.21
		dynamic	HYSPLIT isobaric	0.17	0.14–0.24
0.5°	RMSD	kinematic	mean trajectory	1,800 km	1,400–2,500 km
		dynamic	mean trajectory	320 km	250–450 km
	AHTD	kinematic	HYSPLIT 3D	2,600 km	2,000–3,600 km
		dynamic	HYSPLIT 3D	1,200 km	910–1,600 km
		kinematic	HYSPLIT isobaric	950 km	740–1,300 km
		dynamic	HYSPLIT isobaric	2,800 km	2,200–3,900 km
	RHTD	kinematic	HYSPLIT 3D	2.1	1.6–2.9
		dynamic	HYSPLIT 3D	0.95	0.74–1.3
		kinematic	HYSPLIT isobaric	0.44	0.12–0.21
		dynamic	HYSPLIT isobaric	0.15	0.34–0.61

Table 4.2: Boston reference trajectory measures after eight days.

Resolution	Statistic	Model	Reference	Value	95% CI
0.5°	RMSD	HYSPLIT 3D	mean trajectory	1,200 km	920–1,600 km
		HYSPLIT isobaric	mean trajectory	3,700 km	2,900–5,200 km
	AHTD	HYSPLIT isobaric	HYSPLIT 3D	2,400 km	1,900–3,400 km
	RHTD	HYSPLIT isobaric	HYSPLIT 3D	2.0	1.5–2.7

Table 4.3: Bauru measures of transport deviation after eight days.

Resolution	Statistic	Model	Reference	Value	95% CI
0.25°	RMSD	kinematic	mean trajectory	900 km	700–1300 km
		dynamic	mean trajectory	980 km	760–1400 km
	AHTD	kinematic	HYSPLIT 3D	1,200 km	950–1,700 km
		dynamic	HYSPLIT 3D	1,100 km	860–1,500 km
		kinematic	HYSPLIT isobaric	1,100 km	840–1,500 km
		dynamic	HYSPLIT isobaric	970 km	760–1,300 km
	RHTD	kinematic	HYSPLIT 3D	0.57	0.45–0.80
		dynamic	HYSPLIT 3D	0.54	0.42–0.75
		kinematic	HYSPLIT isobaric	0.55	0.43–0.77
		dynamic	HYSPLIT isobaric	0.49	0.38–0.68
0.5°	RMSD	kinematic	mean trajectory	900 km	700–1,300 km
		dynamic	mean trajectory	350 km	270–490 km
	AHTD	kinematic	HYSPLIT 3D	1,200 km	950–1,700 km
		dynamic	HYSPLIT 3D	1,300 km	1,000–1,800 km
		kinematic	HYSPLIT isobaric	1,100 km	840–1,500 km
		dynamic	HYSPLIT isobaric	1,100 km	860–1,500 km
	RHTD	kinematic	HYSPLIT 3D	0.57	0.45–0.80
		dynamic	HYSPLIT 3D	0.62	0.48–0.86
		kinematic	HYSPLIT isobaric	0.55	0.43–0.77
		dynamic	HYSPLIT isobaric	0.59	0.46–0.82

Table 4.4: Bauru reference trajectory measures after eight days.

Resolution	Statistic	Model	Reference	Value	95% CI
0.5°	RMSD	HYSPLIT 3D	mean trajectory	5,100 km	4,000–7,000 km
		HYSPLIT isobaric	mean trajectory	3,700 km	2,900–5,200 km
	AHTD	HYSPLIT isobaric	HYSPLIT 3D	1,300 km	1,000–1,800 km
	RHTD	HYSPLIT isobaric	HYSPLIT 3D	0.63	0.49–0.87

Table 4.5: Jakarta measures of transport deviation after eight days.

Resolution	Statistic	Model	Reference	Value	95% CI
0.25°	RMSD	kinematic	mean trajectory	550 km	430–770 km
		dynamic	mean trajectory	1,800 km	1,400–2,500 km
	AHTD	kinematic	HYSPLIT 3D	980 km	760–1,400 km
		dynamic	HYSPLIT 3D	830 km	650–1,200 km
		kinematic	HYSPLIT isobaric	1,200 km	900–1,600 km
		dynamic	HYSPLIT isobaric	900 km	700–1,300 km
	RHTD	kinematic	HYSPLIT 3D	0.73	0.57–1.0
		dynamic	HYSPLIT 3D	0.62	0.48–0.86
		kinematic	HYSPLIT isobaric	0.99	0.77–1.4
		dynamic	HYSPLIT isobaric	0.77	0.60–1.1
0.5°	RMSD	kinematic	mean trajectory	550 km	430–770 km
		dynamic	mean trajectory	300 km	230–420 km
	AHTD	kinematic	HYSPLIT 3D	990 km	770–1,400 km
		dynamic	HYSPLIT 3D	670 km	520–930 km
		kinematic	HYSPLIT isobaric	1,200 km	910–1,600 km
		dynamic	HYSPLIT isobaric	740 km	580–1,000 km
	RHTD	kinematic	HYSPLIT 3D	0.74	0.58–1.0
		dynamic	HYSPLIT 3D	0.50	0.39–0.7
		kinematic	HYSPLIT isobaric	1.0	0.78–1.4
		dynamic	HYSPLIT isobaric	0.63	0.49–0.88

Table 4.6: Jakarta reference trajectory measures after eight days.

Resolution	Statistic	Model	Reference	Value	95% CI
0.5°	RMSD	HYSPLIT 3D	mean trajectory	2,200 km	1,700–3,000 km
		HYSPLIT isobaric	mean trajectory	530 km	410–730 km
	AHTD	HYSPLIT isobaric	HYSPLIT 3D	530 km	410–730 km
	RHTD	HYSPLIT isobaric	HYSPLIT 3D	0.39	0.31–0.54

Table 4.7: Barrow measures of transport deviation after eight days.

Resolution	Statistic	Model	Reference	Value	95% CI
0.25°	RMSD	kinematic	mean trajectory	1,100 km	850–1,500 km
		dynamic	mean trajectory	2,400 km	1,800–3,300 km
	AHTD	kinematic	HYSPLIT 3D	480 km	380–670 km
		dynamic	HYSPLIT 3D	610 km	480–850 km
		kinematic	HYSPLIT isobaric	510 km	400–710 km
		dynamic	HYSPLIT isobaric	600 km	470–830 km
	RHTD	kinematic	HYSPLIT 3D	0.24	0.18–0.33
		dynamic	HYSPLIT 3D	0.30	0.23–0.42
		kinematic	HYSPLIT isobaric	0.25	0.20–0.35
		dynamic	HYSPLIT isobaric	0.30	0.23–0.41
0.5°	RMSD	kinematic	mean trajectory	1,100 km	820–1,500 km
		dynamic	mean trajectory	220 km	170–310 km
	AHTD	kinematic	HYSPLIT 3D	490 km	380–680 km
		dynamic	HYSPLIT 3D	130 km	100–190 km
		kinematic	HYSPLIT isobaric	510 km	400–710 km
		dynamic	HYSPLIT isobaric	80 km	61–110 km
	RHTD	kinematic	HYSPLIT 3D	0.24 km	0.19–0.33
		dynamic	HYSPLIT 3D	0.04 km	0.03–0.05
		kinematic	HYSPLIT isobaric	0.25	0.20–0.35
		dynamic	HYSPLIT isobaric	0.04	0.03–0.05

Table 4.8: Barrow reference trajectory measures after eight days.

Resolution	Statistic	Model	Reference	Value	95% CI
0.5°	RMSD	HYSPLIT 3D	mean trajectory	560 km	430–770 km
		HYSPLIT isobaric	mean trajectory	320 km	250–440 km
	AHTD	HYSPLIT isobaric	HYSPLIT 3D	110 km	80–150 km
	RHTD	HYSPLIT isobaric	HYSPLIT 3D	0.05	0.04–0.07

Table 4.9: Reykjavík measures of transport deviation after eight days.

Resolution	Statistic	Model	Reference	Value	95% CI
0.25°	RMSD	kinematic	mean trajectory	1,500 km	1,200–2,100 km
		dynamic	mean trajectory	2,300 km	1,800–3,200 km
	AHTD	kinematic	HYSPLIT 3D	450 km	350–630 km
		dynamic	HYSPLIT 3D	560 km	440–780 km
		kinematic	HYSPLIT isobaric	460 km	360–640 km
		dynamic	HYSPLIT isobaric	520 km	410–730 km
	RHTD	kinematic	HYSPLIT 3D	0.19	0.15–0.26
		dynamic	HYSPLIT 3D	0.24	0.18–0.33
		kinematic	HYSPLIT isobaric	0.19	0.15–0.26
		dynamic	HYSPLIT isobaric	0.21	0.17–0.30
0.5°	RMSD	kinematic	mean trajectory	1,500 km	1,200–2,100 km
		dynamic	mean trajectory	1,800 km	1,400–2,500 km
	AHTD	kinematic	HYSPLIT 3D	420 km	330–590 km
		dynamic	HYSPLIT 3D	730 km	570–1,000 km
		kinematic	HYSPLIT isobaric	440 km	340–610 km
		dynamic	HYSPLIT isobaric	820 km	640–1,100 km
	RHTD	kinematic	HYSPLIT 3D	0.18	0.14–0.25
		dynamic	HYSPLIT 3D	0.31	0.24–0.43
		kinematic	HYSPLIT isobaric	0.18	0.14–0.25
		dynamic	HYSPLIT isobaric	0.17	0.13–0.24

Table 4.10: Reykjavík reference trajectory measures after eight days.

Resolution	Statistic	Model	Reference	Value	95% CI
0.5°	RMSD	HYSPLIT 3D	mean trajectory	340 km	270–480 km
		HYSPLIT isobaric	mean trajectory	410 km	320–570 km
	AHTD	HYSPLIT isobaric	HYSPLIT 3D	400 km	320–560 km
	RHTD	HYSPLIT isobaric	HYSPLIT 3D	0.17	0.13–0.24

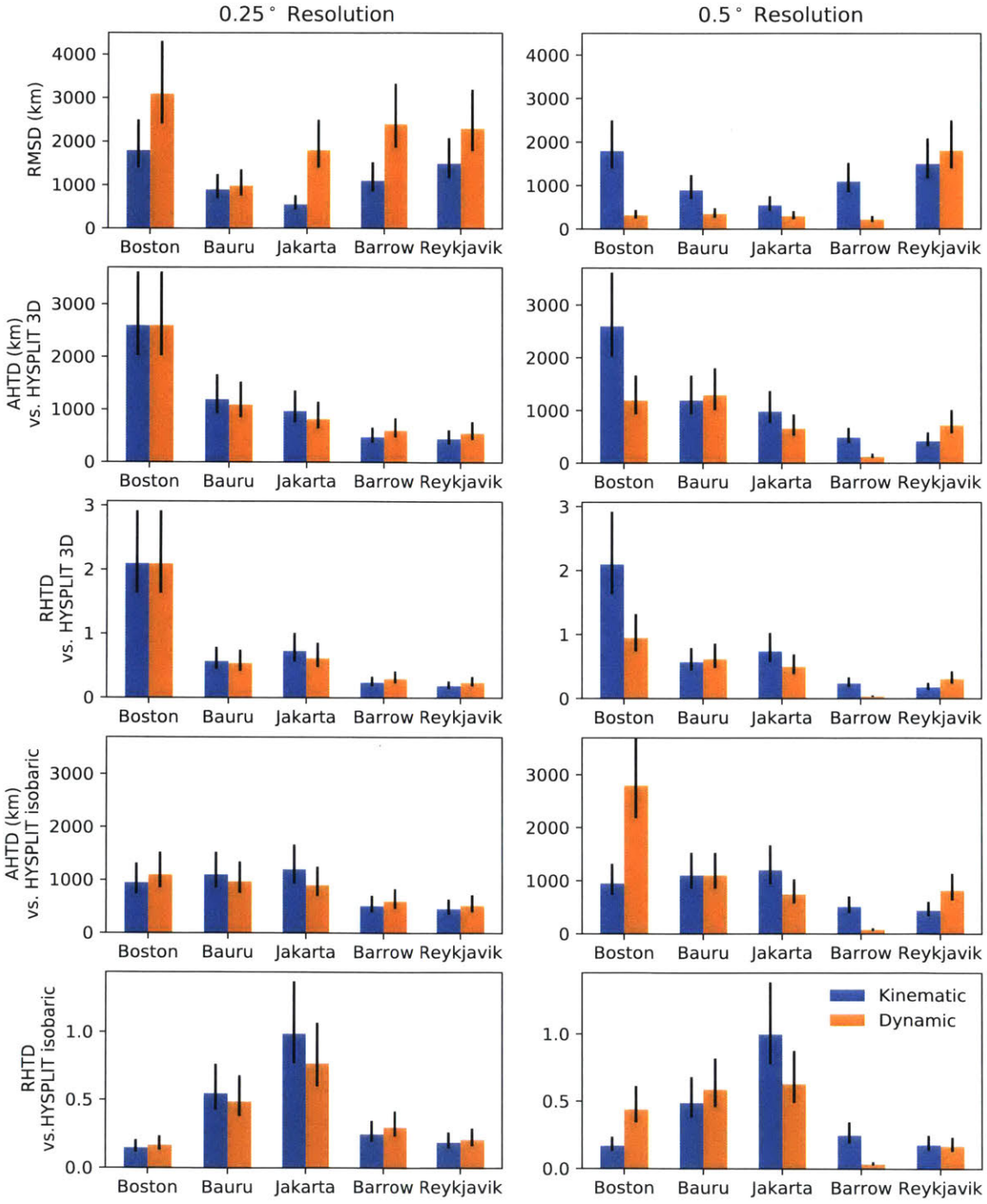

Figure 4-1: A comparison of kinematic and dynamic trajectories using RMSD as well as AHTD and RHTD referenced to 3D and isobaric HYSPLIT trajectories.

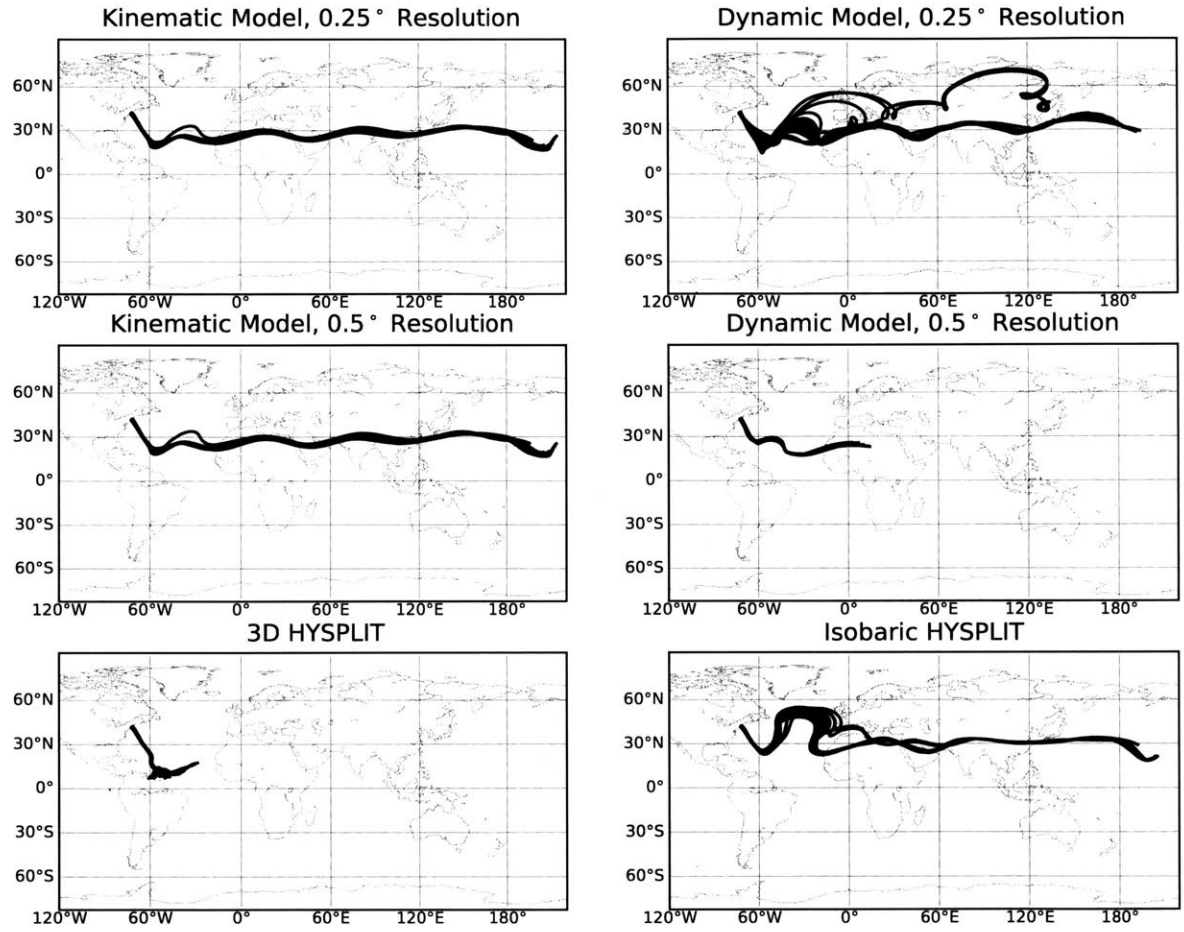

Figure 4-2: Trajectories for parcels launched from Boston, Massachusetts calculated by the experimental and reference models.

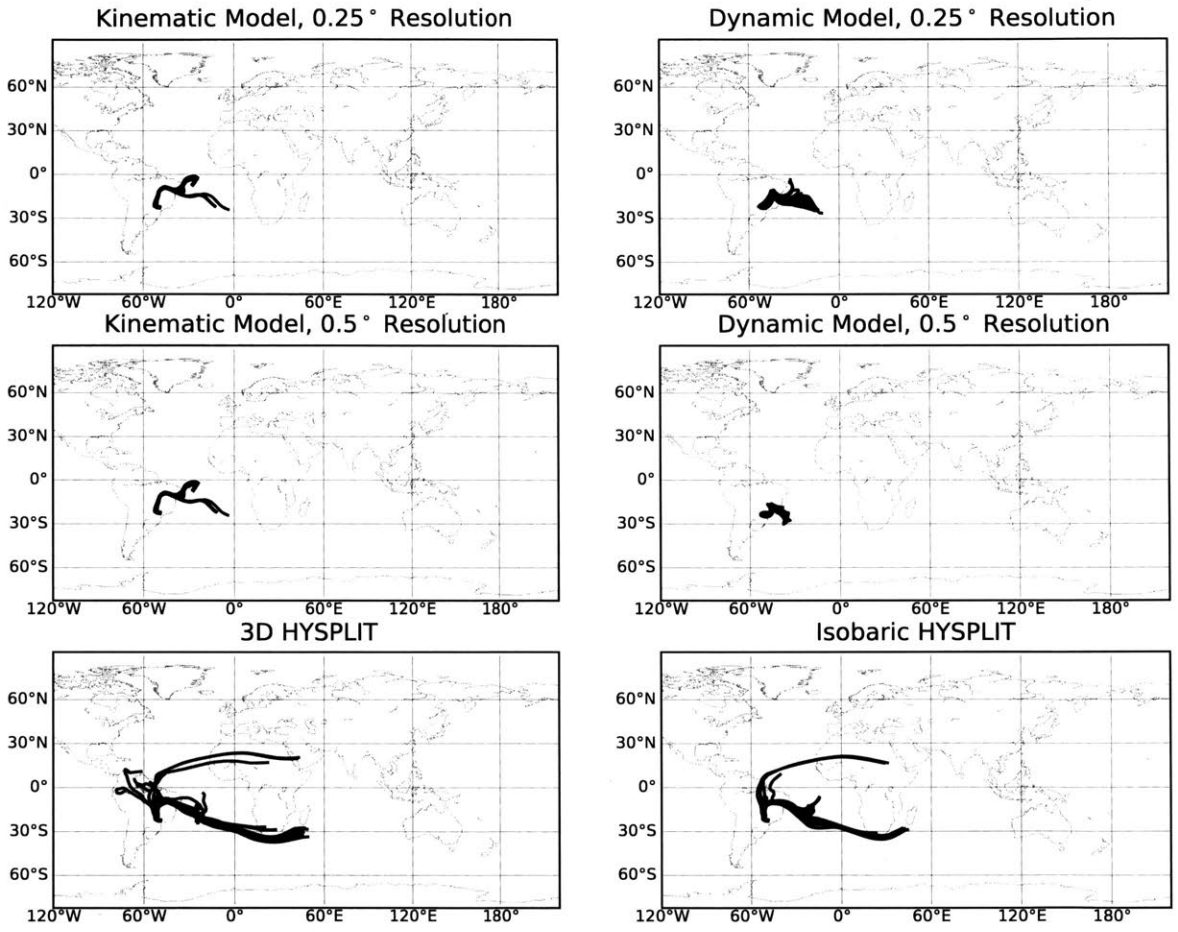

Figure 4-3: Trajectories for parcels launched from Bauru, Brazil calculated by the experimental and reference models.

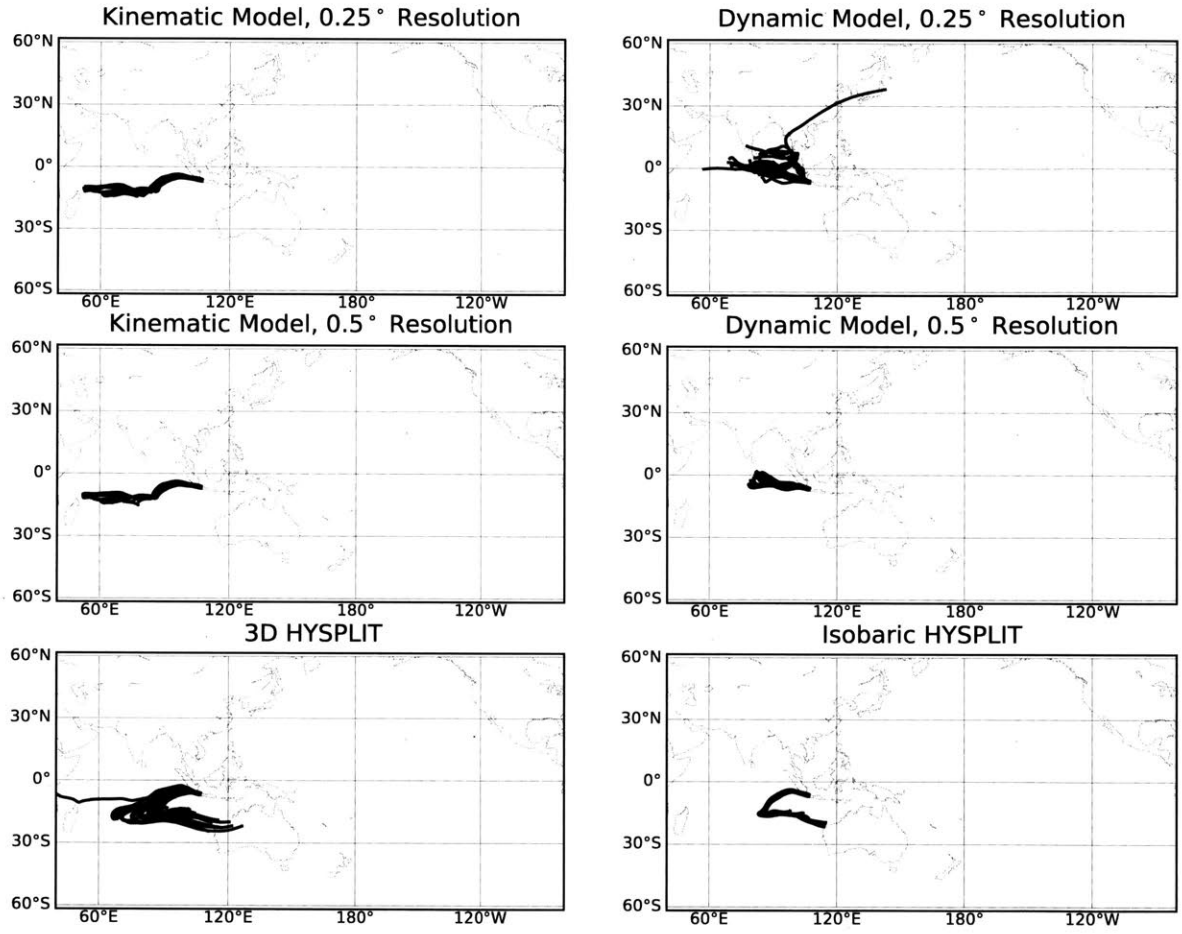

Figure 4-4: Trajectories for parcels launched from Jakarta, Indonesia calculated by the experimental and reference models.

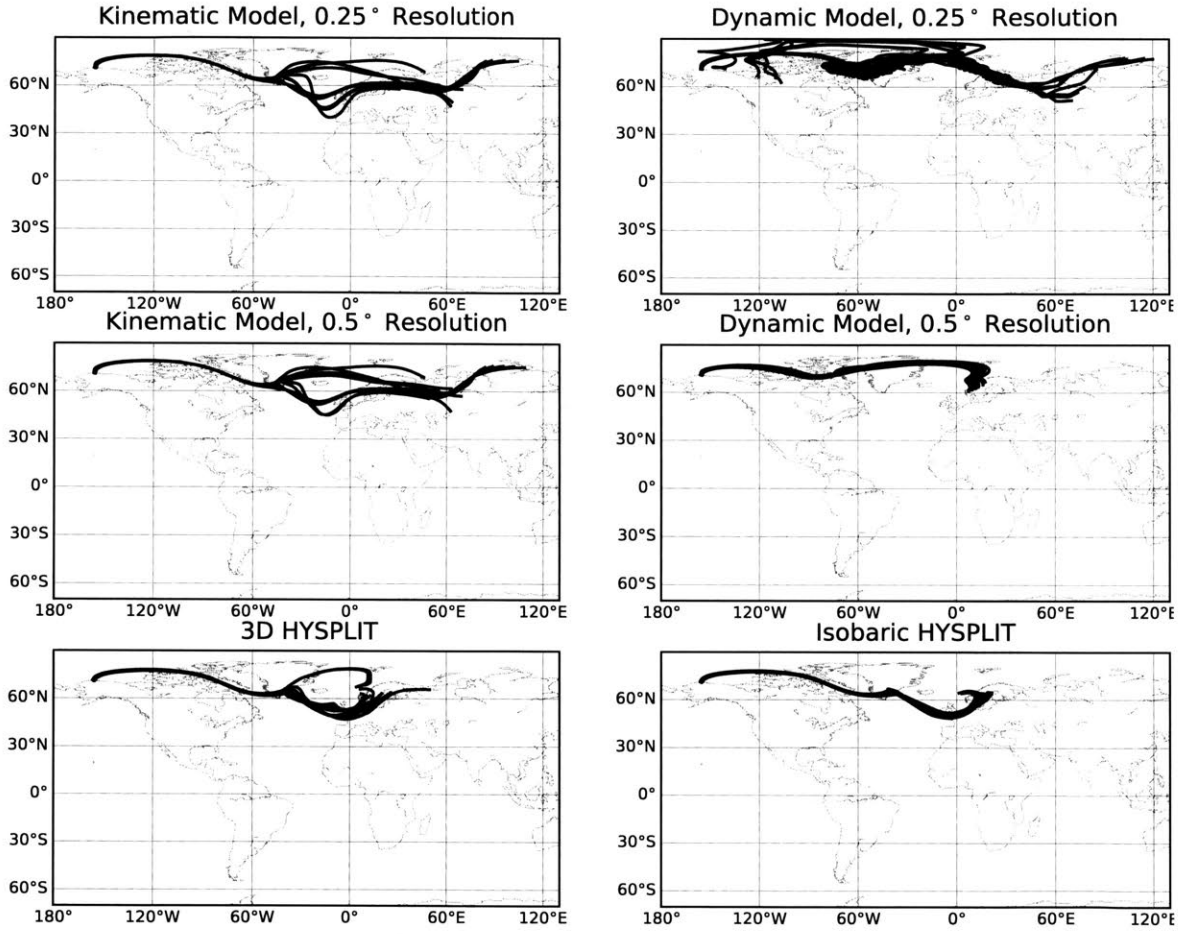

Figure 4-5: Trajectories for parcels launched from Barrow, Alaska calculated by the experimental and reference models.

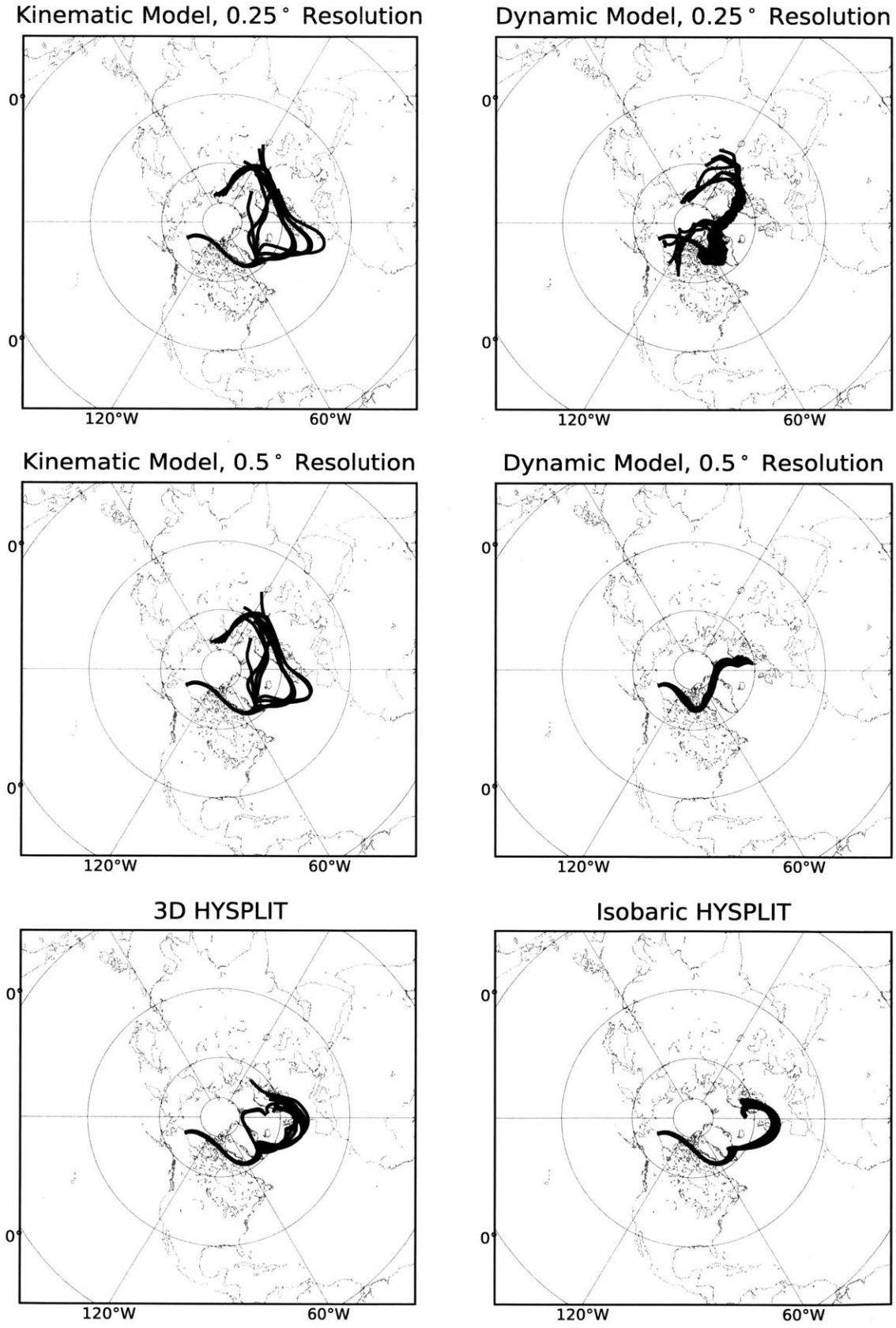

Figure 4-6: Polar stereographic maps of trajectories from Barrow, Alaska.

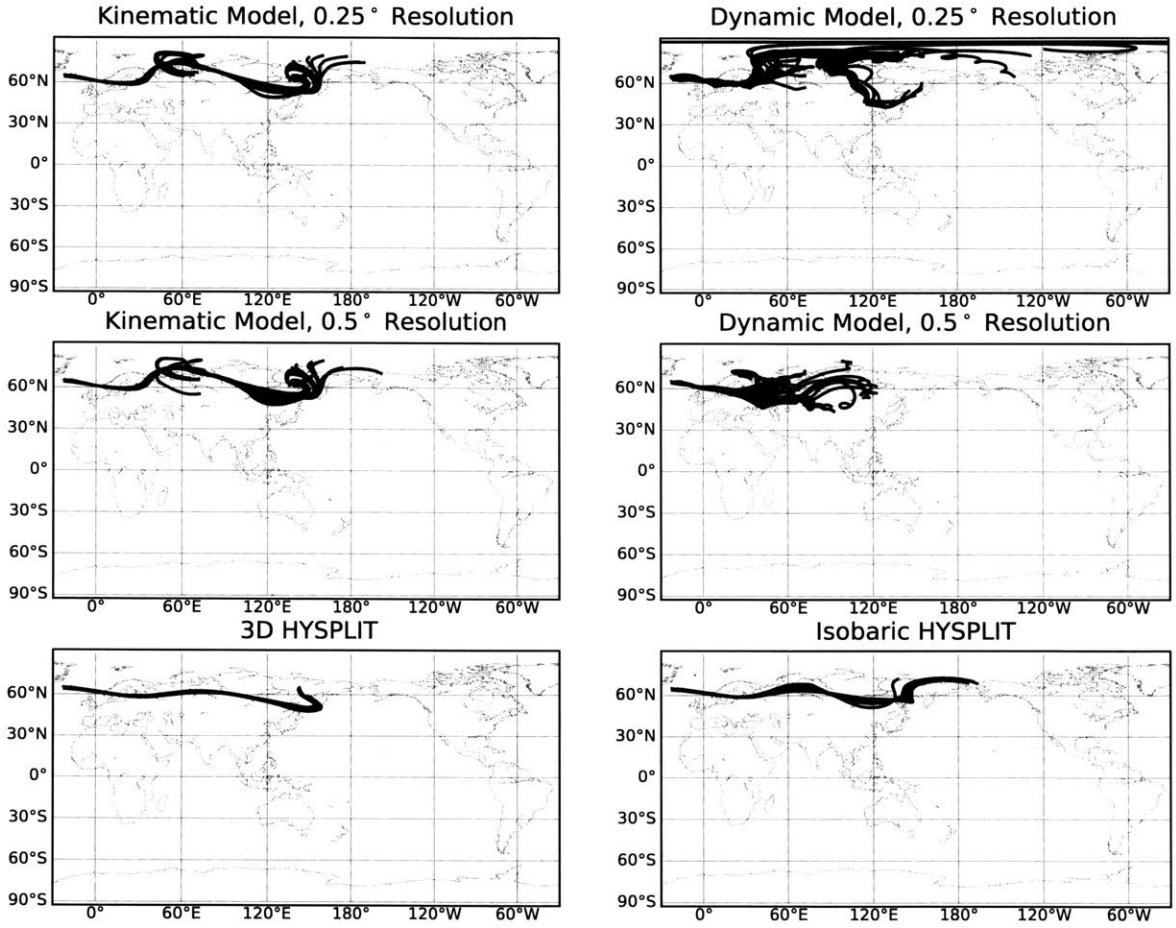

Figure 4-7: Trajectories for parcels launched from Reykjavík, Iceland calculated by the experimental and reference models.

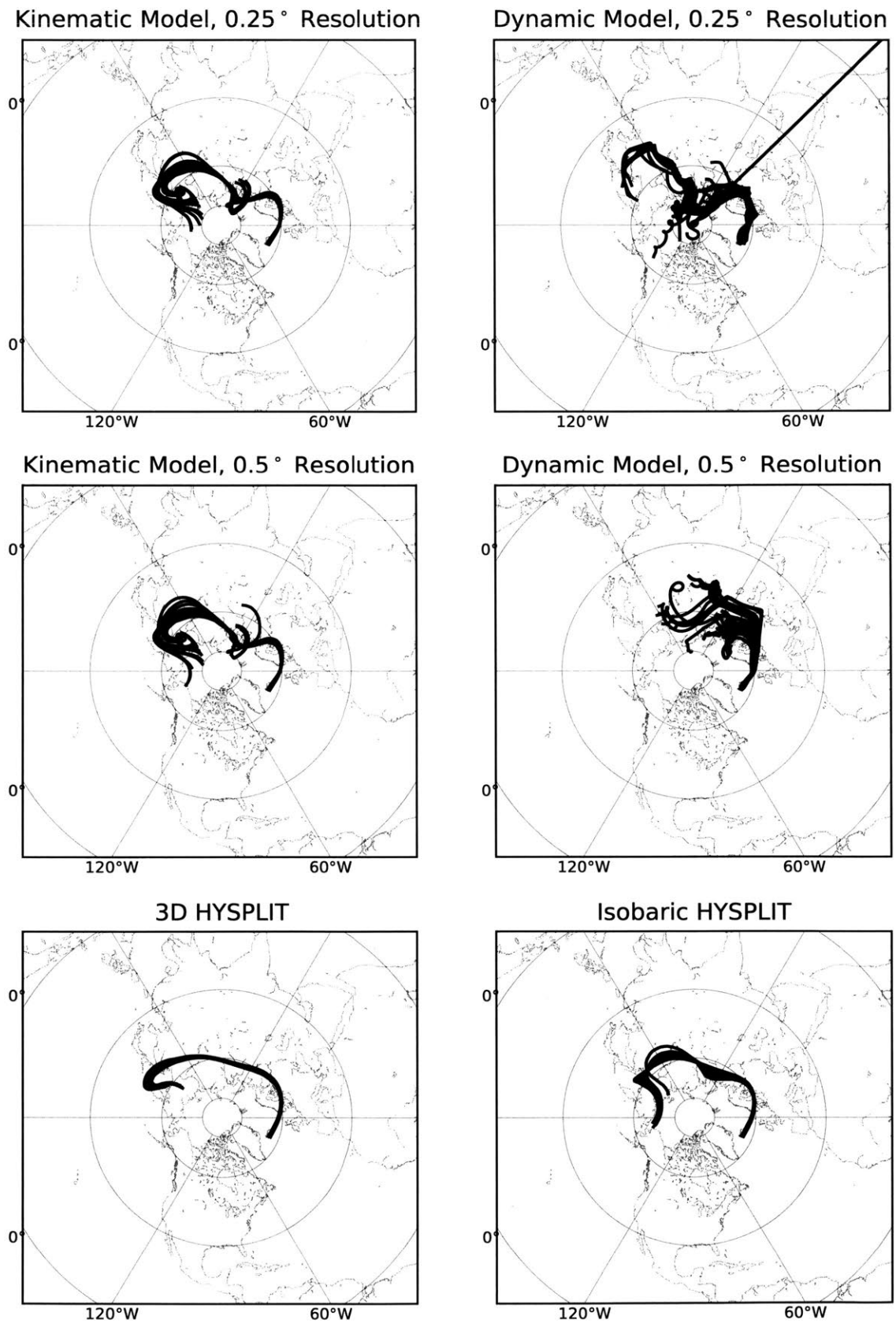

Figure 4-8: Polar stereographic maps of trajectories from Reykjavík, Iceland.

5 Discussion

Performance varies among locations as a result of different atmospheric flow regimes in each part of the globe. Overall, dynamic trajectories perform comparably to kinematic trajectories.

The dynamic model is sensitive to changes in the spatial resolution of input geopotential height values. The kinematic model, on the other hand, produces trajectories that are almost identical using the two chosen wind speed resolutions. Dynamic trajectories calculated with the coarser 0.5° grid manifest slower wind speeds than those calculated with the 0.25° grid. The coarser grid has the effect of smoothing out steep geopotential height gradients which lead to high wind speeds.

The relatively large deviation between the HYSPLIT 3D and isobaric models demonstrates the importance of vertical modeling to trajectory calculations. Even an optimal two dimensional model will deviate significantly from real atmospheric trajectories. This is obvious in the case of Boston, where trajectories from the 3D HYSPLIT run remain north of South America, while in every other model run they flow east into the subtropical jet. Another feature apparent in the Boston trajectory map is the spiraling behavior of some trajectories in the dynamic model with 0.25° resolution. These may be inertial circles that have not been damped by the weak friction term in the model. The spiraling trajectories are in the mid-latitudes, where eddies have been shown to form in Figure 2-2. It is possible that these spirals describe potential behavior of real parcel trajectories that the kinematic and coarser dynamic models smooth out. It is hard to tell from this analysis whether the spirals predict real flow patterns or represent artificial ageostrophic oscillations.

The trajectory maps from Barrow and Reykjavík show unrealistic trajectory be-

havior from the 0.25° dynamic model at high latitudes. Near the poles, these dynamic trajectories are observed tracing tight spirals which are not reflected in any other model runs. They do not affect the overall path of the parcel much: measures of deviation are low for dynamic trajectories from Barrow and Reykjavík. This implies that near the poles, dynamic trajectories are looping around kinematic trajectories: drawing a path through the center of the spiral will probably approximate a kinematically-calculated trajectory. The Coriolis parameter is strongest near the poles, so oscillations here can be expected to be the most resistant to damping.

6 Conclusions

The analysis suggests that isobaric dynamic models perform comparably to isobaric kinematic models at predicting trajectories over an eight-day timescale. Adding a term to the dynamic model to represent the force of friction greatly reduces, but does not eliminate, unrealistic spirals in the trajectories. In the dynamic model with friction, undamped spirals remain in trajectories from the mid-latitudes to the poles.

Future work might explore these oscillations. Observational data could be analyzed to determine whether any oscillatory behavior is present in real atmospheric trajectories. If oscillations are sometimes present in the atmosphere, dynamic models may be better suited to preserve this behavior that kinematic models smooth out. The time resolution of gridded wind speeds output by forecast models may not be fine enough to resolve small-scale inertial circles. A particular regime in which kinematic models might artificially smooth spiraling motion is the mid-latitude bands in which rotating weather systems form. Determining how kinematic and dynamic trajectories compare at modeling flow in eddies is a potential direction for future research. If oscillations are not observed, it implies that something is out of sync between the balance of forces in the real atmosphere and the balance of forces in the trajectory model. Possible sources of error include the linear interpolation of the geopotential gradient, effects from vertical motion which are neglected in isobaric models, and an inaccurately described force of friction.

This study did not explore in depth how the force of friction is modeled. Future work might examine the behavior of dynamic models for different values of the friction parameter. Another direction is to develop alternate expressions for friction besides the ageostrophic wind speed times a constant friction parameter. In particular, a

continuous friction expression that does not become unrealistic near the Equator would be valuable.

For the studied timestep and time resolution of the data, the dynamic trajectory model is more sensitive to changes in spatial resolution than the kinematic model. When a dynamic trajectory model is implemented, it should be tested with a range of data resolutions and compared to observational or other model data to determine the resolution that produces the most accurate trajectories. With the right choice of spatial resolution and expression for the force of friction, dynamic trajectories are suitable for demonstrating the paths of air parcels in the atmosphere.

Bibliography

[Bowman et al., 2013] Bowman, K., Lin, J. C., Stohl, A., Draxler, R., and Konopka, P. (2013). Input data requirements for Lagrangian trajectory models. *Bulletin of the American Meteorological Society*, 94(7):1051–1058.

[Draxler and Hess, 1997] Draxler, R. R. and Hess, G. D. (1997). Description of the HYSPLIT_4 modeling system. Technical report, NOAA Air Resources Laboratory, Silver Spring, MD.

[Kuo et al., 1985] Kuo, Y., Skumanich, M., Haagenson, P. L., and Chang, J. S. (1985). The Accuracy of Trajectory Models as Revealed by the Observing System Simulation Experiments. *Monthly Weather Review*, 113:1852–1867.

[Marshall and Plumb, 2008] Marshall, J. and Plumb, R. A. (2008). *Atmosphere, Ocean, and Climate Dynamics: An Introductory Text*, volume 93 of *International Geophysics Series*. Elsevier Academic Press.

[NOAA, 2004] NOAA (2004). Global Data Assimilation System (GDAS1) Archive Information. Technical report, NOAA-Air Resources Laboratory, Silver Spring, MD.

[Petterssen, 1940] Petterssen, S. (1940). *Weather Analysis and Forecasting*. McGraw-Hill Book Company, New York.

[Rolph and Draxler, 1990] Rolph, G. D. and Draxler, R. R. (1990). Sensitivity of Three-Dimensional Trajectories to the Spatial and Temporal Densities of the Wind Field. *Journal of Applied Meteorology*, 29:1043–1054.

[Rolph et al., 2017] Rolph, G. D., Stein, A. F., and Stunder, B. J. B. (2017). Real-time Environmental Applications and Display sYstem: READY. *Environmental Modelling & Software*, 95:210–228.

[Saraceno et al., 2015] Saraceno, T., Kinney, L., Illari, L., and McKenna, W. D. (2015). Aerocene: Becoming Aerosolar. *The Aerocene Newspaper*, pages 14–15.

[Sinnott, 1984] Sinnott, R. W. (1984). Virtues of the Haversine. *Sky & Telescope*, 68(2):159.

[Stein et al., 2015] Stein, A. F., Draxler, R. R., Rolph, G. D., Stunder, B. J. B., Cohen, M. D., and Ngan, F. (2015). NOAA's HYSPLIT Atmospheric Transport and Dispersion Modeling System. *Bulletin of the American Meteorological Society*, 96:2059–2077.

[Stohl, 1998] Stohl, A. (1998). Computation, accuracy and applications of trajectories—a review and bibliography. *Atmospheric Environment*, 32(6):947–966.

[Stohl and Seibert, 1998] Stohl, A. and Seibert, P. (1998). Accuracy of trajectories as determined from the conservation of meteorological tracers. *Quarterly Journal of the Royal Meteorological Society*, 124:1465–1484.